Asian Journal of Chemistry; Vol. 36, No. 10 (2024), 2431-2442

ASIAN JOURNAL OF CHEMISTRY

https://doi.org/10.14233/ajchem.2024.32553

Flexible PVP/PEO/MnO_2 Polymer Nanocomposites based Cathode Material for Asymmetric Supercapacitor

W. Maria Therease Ramya[1,2], K. Venkatachalam[1,*], A. Murugan[3,4], M. Anandha Jothi[5] and S. Thangarasu[6,*]

[1]Department of Physics, Government Arts College (Autonomous), Coimbatore-641018, India
[2]Department of Physics, Nirmala College for Women (Autonomous), Coimbatore-641018, India
[3]Center for Energy and Environment, Karpagam Academy of Higher Education, Coimbatore-641021, India
[4]Department of Science and Humanities, Karpagam College of Engineering, Coimbatore-641032, India
[5]Department of Physics, P.S.R. Engineering College, Sivakasi-626140, India
[6]Department of Physics, Kalasalingam Academy of Research and Education, Krishnankoil-626126, India

*Corresponding authors: E-mail: vkgaccbe@gmail.com; sthangarasu@gmail.com

Received: 12 August 2024; *Accepted*: 16 September 2024; *Published online*: 30 September 2024; AJC-21775

The solution casting method has been used to design a polymer nanocomposite (PNC) based on polyvinylpyrrolidone (PVP), polyethylene oxide (PEO) and manganese dioxide nanoparticles (MnO_2 NPs) at different concentrations. The effective integration of MnO_2 NPs in the PVP/PEO blend matrix has been characterized by Fourier transform infrared spectroscopy (FTIR) and powder X-ray diffraction (XRD). An XRD study has demonstrated that adding MnO_2 nanoparticles up to 1 wt.% of MnO_2 increases the crystallinity of polymer nanocomposites. As the wt.% MnO_2 NPs grew from 0.25 to 1 at room temperature, the values of ε′ increased from 12.5 to 112.5 at 42 Hz and the value of ε″ increased to 1656 at ambient temperature and then to 20752 at 373 K for 1 wt.% MnO_2. Asymmetric supercapacitor (ASC) has been fabricated and its electrochemical performance has been evaluated. All CV curves exhibited a non-rectangle shape even at a high scan rate of 100 mV s^{-1} for all ASC devices, suggesting the good capacitive behaviours of PNC electrodes.

Keywords: Polymer nanocomposites, PVP/PEO, Electrode, Asymmetric supercapacitor, Charge-discharge.

INTRODUCTION

Polymer nanocomposites (PNC) have sparked significant industry and research interest due to their remarkable applicability in a variety of fields and are projected to be one of the most helpful functions for future nanotechnology developments. PNC consists of a polymer matrix integrated with various nanofillers, which are uniformly dispersed throughout [1-3]. This composition offers unique benefits that cannot be achieved by the individual components acting independently. Nanofillers improve the properties of polymeric substances, perhaps making them suitable for improved energy storage systems. Polymer nanocomposites look to have a promising future for many applications due to low-cost and simplicity of production, which make our lives easier. Many factors must be considered when designing and fabricating polymer-based nanocomposite electroactive materials for supercapacitor applications, including material selection, fabrication process parameters, interfacial characteristics, electrical conductivity and surface area, among others [4,5]. Despite substantial progress in developing nanocomposite electroactive materials for supercapacitor applications, several obstacles remain.

Supercapacitors, sometimes referred to as electrochemical capacitors, are the energy storage devices with a high power density and quick charge/discharge rates that fill the gap between batteries and conventional capacitors. There is a growing interest in creating cutting-edge electrode materials to improve the performance of supercapacitors due to the growing need for effective energy storage solutions in a variety of applications, including portable devices, electric vehicles and renewable energy systems [6,7]. Promising options for supercapacitor electrodes are polymer materials such as polyvinylpyrrolidone (PVP) and polyethylene oxide (PEO), which are noted for their superior film-forming abilities, high flexibility and good ionic conductivity [8-10]. Because of the synergistic effects between the polymer matrix and the active material, it is possible to

further improve the electrochemical performance of supercapacitors by adding transition metal oxides, *e.g.* manganese dioxide (MnO_2), into PVP-PEO matrices. Due to its high specific capacitance, affordability and environmental friendliness, MnO_2 is a highly researched pseudocapacitive material that is a popular option for supercapacitor applications [11,12]. MnO_2 can enhance supercapacitors' total energy storage capacity, cycling stability and charge-discharge efficiency when paired with PVP-PEO, providing a viable remedy for the problems facing energy storage technology at the moment.

In this study, we examine the synthesis, properties and electrochemical behaviour of PVP-PEO composites containing MnO_2 for supercapacitor uses. The objective is to demonstrate the feasibility of utilizing PVP-PEO in conjunction with MnO_2 as an advanced electrode material to enhance supercapacitor performance and contribute to the development of next generation energy storage devices through an exploration of the synergistic interactions between the polymer matrix and the transition metal oxide.

EXPERIMENTAL

To synthesize polymer nanocomposites, the chemicals *viz.* manganese(III) acetate dihydrate (Sigma-Aldrich), citric acid (Sigma-Aldrich) and polyethylene oxide (PEO) with a molecular weight of Mw = 1,00,000 g/mol (Sigma-Aldrich), Poly(vinyl pyrrolidone) PVP with a molecular weight of Mw = 130,000 g/mol (Sigma-Aldrich) were procured. Furthermore, MnO_2 nanoparticles were synthesized by the sol-gel method [13].

Preparation of polymer nanocomposites (PNCs): Polymer nanocomposites were made utilizing the solution casting process. The different weight percentages of MnO_2 NPs were incorporated with poly(vinyl pyrrolidone) PVP and poly(ethylene oxide) (PEO). The PVP and PEO were dissolved in 30 mL of double distilled water. Following 4 h of stirring at room temperature, the solutions of PVP and PEO yield a uniform, viscous blend that requires dropwise incorporation for optimal mixing. In order to add different wt.% MnO_2 NPs (x = 0.25, 0.5, 0.75 and 1 wt.%) dropwise in 10 mL of double distilled water and stir for 8 h at room temperature, the blended solution was stirred for more than 3 h. Following that the polymer nanocomposites were allowed to dry at room temperature in a plastic petri dish containing the uniform, viscous solution. Finally, the prepared PNCs were subjected to various characterizations.

Characterization: The structure of polymer nanocomposites (PNCs) was examined using X-ray diffraction patterns obtained with a Bruker D8 advanced X-ray diffractometer. The functional group was found using a Shimadzu IR Tracer-100 spectrometer. The electrochemical measurements were performed using a two-electrode setup from the CHI model 660E electrochemical workstation. Dielectric and conductance studies were measured by HIOKI 3536 LCR metre.

RESULTS AND DISCUSSION

Structural studies: The XRD patterns of blend complexes with various weight percentages of MnO_2 nanoparticles are shown in Fig. 1. The distinctive peaks of the prepared nanoparticles matched β-MnO_2 and were indexed with JCPDS card no. 024-0735. The PVP is completely amorphous and does not form crystalline peaks, whereas the wider characteristics of PEO are appeared at 18.3º and 23.4º, confirmed the production of polymer composites [8]. The strength of this peak increased with the amount of MnO_2 indicating that blended PNCs were generated. The absence of characteristic diffraction peaks for MnO_2 in the XRD templates of mix PNCs was most likely due to the low level of MnO_2. Fig. 2 displays the FT-IR spectra of MnO_2 and PEO/PVP/MnO_2 nanocomposites at 4000-400 cm^{-1}. The OH stretching mode was responsible for the strong band at 3400 cm^{-1} observed in all PNCs [8]. The peak of the C=O group was appeared 1632 cm^{-1}, which is ascribed to the stretching of PVP. The peaks in the 1380-1270 cm^{-1} region were due to the presence of CH_2 asymmetric bending and symmetric twisting. The asymmetry CH stretching of CH_2 group appears

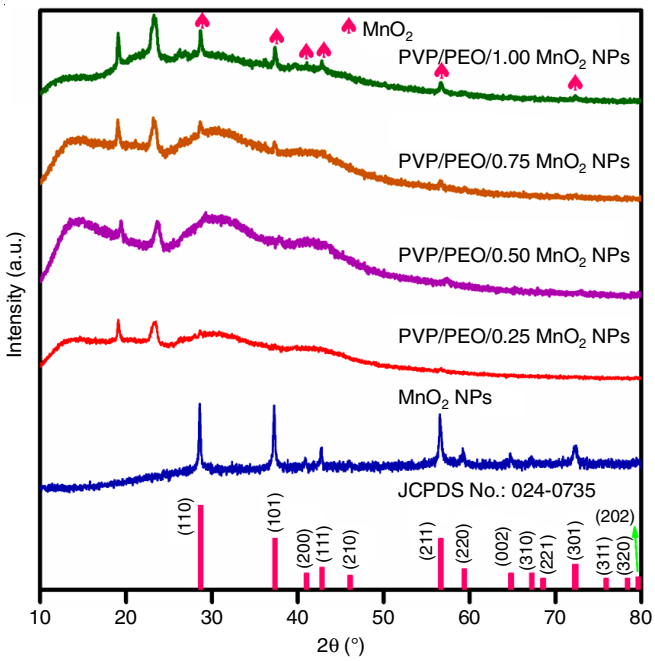

Fig. 1. XRD patterns of MnO_2 nanoparticles and PVP/PEO/MnO_2

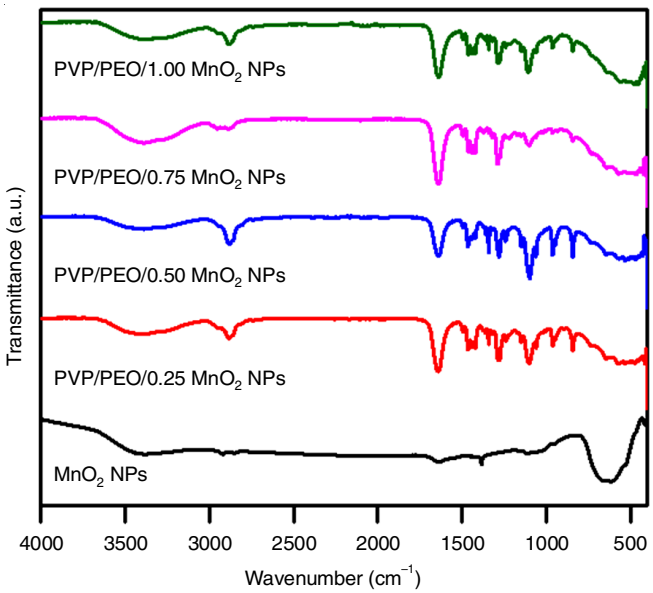

Fig. 2. FTIR spectra of MnO_2 nanoparticles and PVP/PEO/MnO_2

in the region at 2823 cm^{-1} [14]. The modest peak at 1456 cm^{-1} is due to the CH_2 scissoring mode of PEO molecule. A peak at 878 cm^{-1} is due to the CH_2 rocking mode of PVP and C-O stretching in PEO [8]. The FT-IR analysis shows that no interactions occur between the (PEO-PVP) blend and MnO_2 NPs.

Complex impedance analysis: The Nyquist plot helps to understand the properties of materials that are inductive, capacitive and resistive. The Nyquist plots for various composition of 30 wt.% PEO/70 wt.% PVP/0.25 to 1 wt.% MnO_2 at room temperature and 30 wt.% PEO/70 wt.% PVP/1 wt.% MnO_2 at 303 to 373 K temperature are shown in Fig. 3a-b. The results show that the semi-circle shrinks with increasing temperature and wt.% MnO_2 indicating a steady decrease in compound resistance. The amplitude of the real and imaginary parts of the impedance is significantly impacted by this resistance value. A suitable equivalent circuit for this is given in Fig. 3c.

The circuit has a constant phase element (CPE) as a result of the non-ideal capacitive behaviour [15]. Using the following formula, one can determine a sample's conductivity (σ) based on its bulk resistance (R_b).

$$\sigma = \frac{t}{R_b A}(S/cm)$$

where the thickness and area of the samples are denoted by t and A, repectively. Table-1 presents the measured conductivity values for the samples. Increasing the wt.% of MnO_2 samples to improve charge carrier availability, hence elevating the conductivity of material. The conductivity for 1 wt.% MnO_2 samples raises with the increases of temperature due to the thermally activated conduction mechanisms [16].

Dielectric properties: Non-destructive technique of complex impedance spectroscopy used to help to understand the relation between the dielectric properties and micro-structure of materials. Four variables were obtained as a function of frequencies which is phase angle, real & imaginary impedance and the dielectric loss.

The complex permittivity:

TABLE-1
CONDUCTIVITY OF FOR VARIOUS (0.25 to 1) wt.% MnO_2 AND 1 wt.% MnO_2 BASED POLYMER ELECTRODE AT ROOM TEMPERATURE AND VARIOUS TEMPERATURE

Conductivity value for PVP/PEO//X wt.% MnO_2 at 303 K	
X wt.% MnO_2 sample	Conductivity (S/cm)
0.25	4.16×10^{-10}
0.50	1.28×10^{-9}
0.75	1.09×10^{-8}
1.00	1.86×10^{-8}
Conductivity value for PVP/PEO//1 wt.% MnO_2 at different temp.	
Temperature	Conductivity (S/cm)
313	2.48×10^{-8}
333	6.28×10^{-8}
353	1.57×10^{-7}
373	2.73×10^{-7}

$$\varepsilon^* = \varepsilon' - j\varepsilon''$$

$$\left|\varepsilon^*\right| = \sqrt{\varepsilon'^2 + \varepsilon''^2}$$

The relative permittivity/dielectric constant (ε′), dielectric loss (ε″) and dielectric energy dissipation factor (tan δ) were calculated from complex impedance (Z^*)

$$Z^* = Z' - jZ''$$

$$\text{Since, } \varepsilon' = \frac{t}{\omega A \varepsilon_0} \times \frac{-Z''}{Z'^2 + Z''^2} \text{ \& } \varepsilon'' = \frac{t}{\omega A \varepsilon_0} \times \frac{Z''}{Z'^2 + Z''^2}$$

Dielectric energy dissipation factor:

$$\tan\delta = \frac{\varepsilon''}{\varepsilon'}$$

where ω = angular frequency (2πf) in hertz, A = area of the polymer electrode film (m^2); t = thickness of polymer electrode film (m), ε_0 = vacuum permittivity (8.854×10^{-12} F/m), Z′ = Real impedance (ohm); Z″ = imaginary impedance (ohm).

The dielectric constant plots of 30 wt.% PEO/70 wt.% PVP/0.25 to 1 wt.% MnO_2 electrode film at room temperature and 30 wt.% PEO/70 wt.% PVP/1 wt.% MnO_2 electrode at

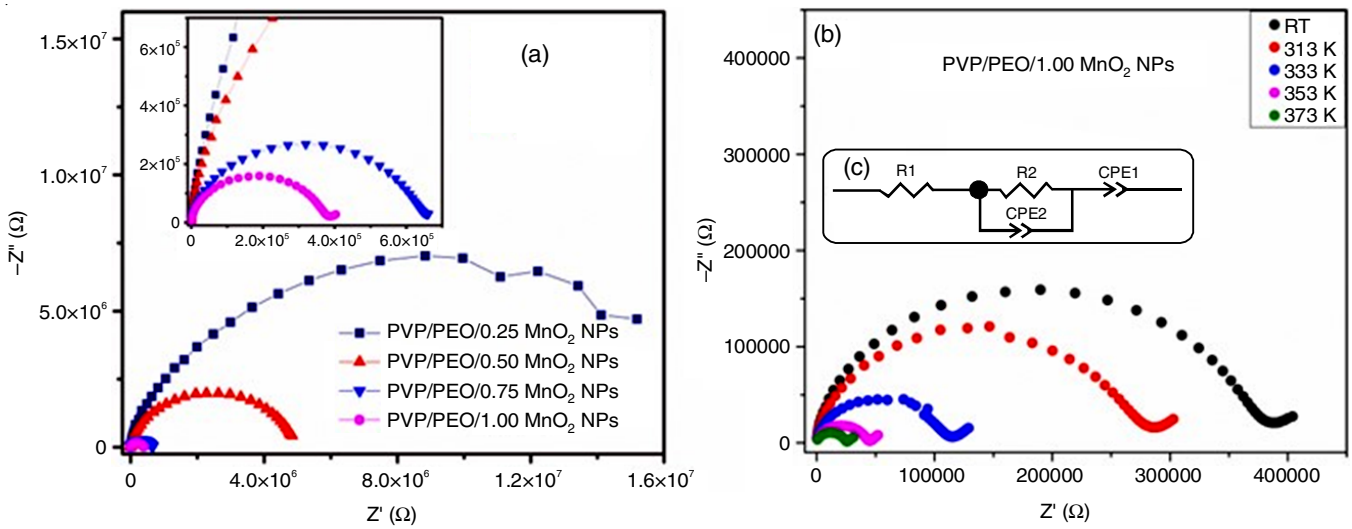

Fig. 3. Nyquist plot of PVP/PEO/0.25 to 1 wt.% MnO_2 electrode film (a) at 303 K, (b) PVP/PEO/1 wt.% MnO_2 electrode film at various temperature and (c) equivalent circuit

various temperatures are displayed in Fig. 4a-b, respectively, within the frequency range of 42 Hz to 1000 kHz. A significant dielectric dispersion caused by the Maxwell-Wagner type interfacial polarization is shown by the high dielectric constant at low frequencies and the low dielectric constant at high frequencies [17]. The dielectric constant gradually dcreases in frequency from 42 to 1000 Hz in the presence of various polarizations, including electronic, ionic, dipole, atomic, space charge, *etc*. It is nearly constant above 1000 Hz. Due to the frequency increment, the interface dipoles cannot have enough time to turn in response to the applied alternating electric field [18]. As the wt.% MnO_2 increases from 0.25 to 1 at room temperature, the values of ε′ increased from 12.5 to 112.5 at 42 Hz. Due to thermally activated conducting ion motion, its values grew even more, reaching a value of 3878 when the temperature rise to 373 K for 1 wt.% MnO_2. Similar behaviour were observed in the dielectric loss (ε″) of 30 wt.% PEO/70 wt.% PVP/0.25 to 1 wt.% MnO_2 electrode (Fig. 5a) and 30 wt.% PEO/70 wt.% PVP/1 wt.% MnO_2 electrode (Fig. 5b). The value of ε increases to 1656 at ambient temperature and then to 20752 at 373K for 1 wt.% MnO_2.

Real and imaginary modulus: The electrical transport mechanism and dielectric relaxation processes can be better understood through the complex analysis of dielectric modulus. The complex modulus (M^*):

$$M^* = \frac{1}{\varepsilon^*} = j\omega C_0 Z^* = M' + jM''$$

where geometric capacitance $C_0 = \frac{\varepsilon_0 A}{t}$

$$M' = \frac{\varepsilon'}{\varepsilon'^2 + \varepsilon''^2} \text{ (real part) and } M'' = \frac{\varepsilon''}{\varepsilon'^2 + \varepsilon''^2} \text{ (imaginary part)}$$

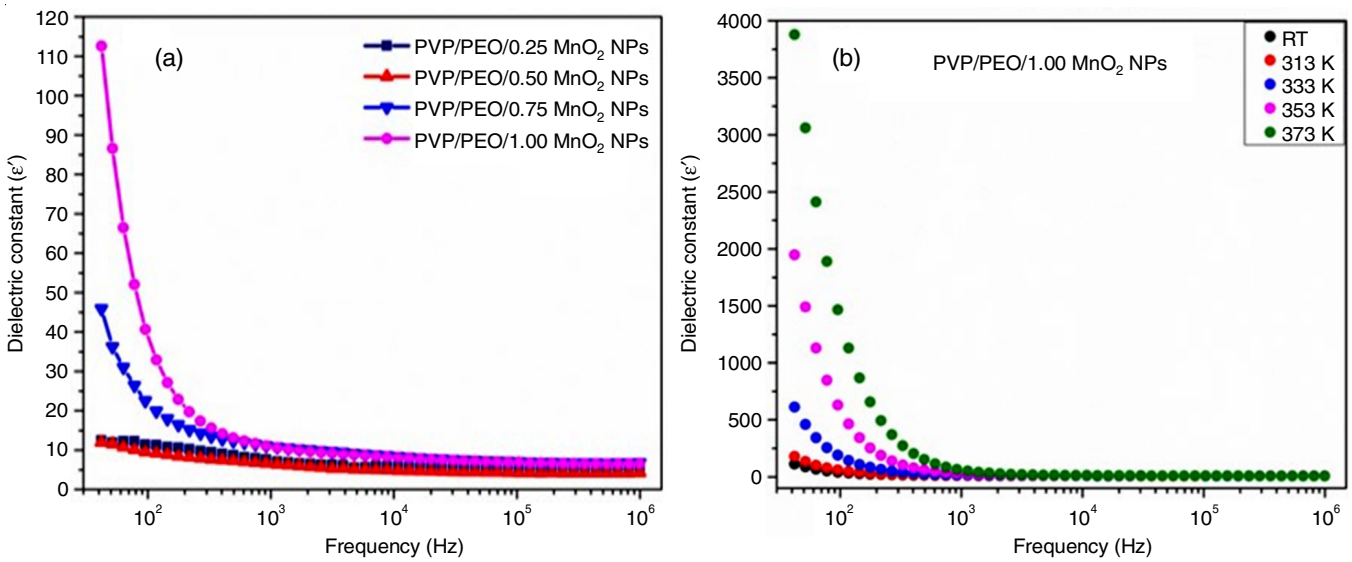

Fig. 4. Dielectric constant *versus* frequency of PVP/PEO/0.25 to 1 wt.% MnO_2 electrode film (a) at 303 K and (b) PVP/PEO/1 wt.% MnO_2 electrode film at various temperature

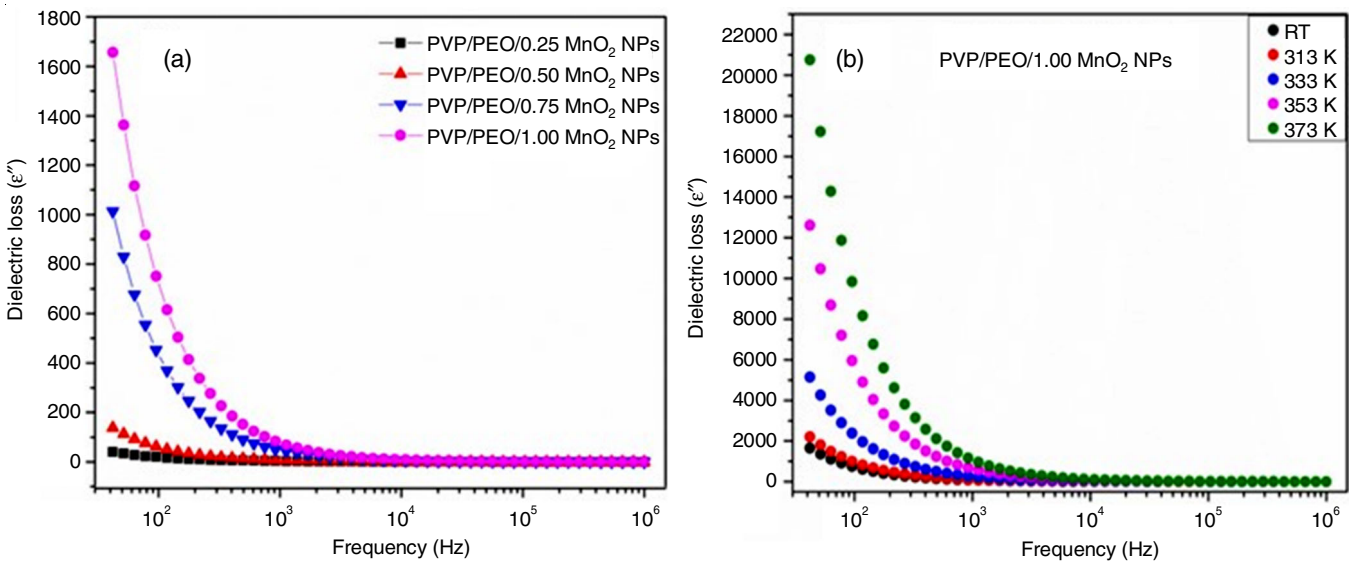

Fig. 5. Dielectric loss of PEO/PVP/0.25 to 1 wt.% MnO_2 electrode film (a) at 303 K and (b) various temperature

The changes in the real part of module M′ as a function of frequencies for various wt.% MnO_2 added PVP/PEO based polymer electrode films at room temperature and PEO/PVP/1 wt.% MnO_2 electrode film at various temperature are displayed in Fig. 6a-b, respectively. At low frequencies, the M′ value is almost zero. For samples containing 0.25 wt.% to 1 wt.% MnO_2, the increase in charge carriers causes this region to expand from 42 Hz to 1000 Hz. Then M′ continuously raised to reach saturation after at 7000 Hz to 10^5 Hz, which is achieved by the conduction mechanism of available mobile charge carriers [19]. However, increase the temperature the zero level of low frequency region and saturation regions are shift towards the higher frequency region as observed from Fig. 6b. This is occurring because of presence of more voids/elongation of polymer chains by application of temperature.

Fig. 7a-b exhibit the variation of imaginary part of module M″ *versus* frequency of different wt.% MnO_2 added PVP/PEO based Polymer electrode films. Low frequency region $(2\pi f_{max}^{M''}\tau_{M''} < 1)$, high frequency region $(2\pi f_{max}^{M''}\tau_{M''} > 1)$ and maximum/top frequency region $(2\pi f_{max}^{M''}\tau_{M''} = 1)$ of three regions observed from this M″ plot. The charge carriers at low frequency move long distances through the hopping mechanism. The charge carriers at high frequency move over short distances by imprisoned charge carriers to make localized movement inside the potential wells [20]. At maximum point transition occur from long to short distance mobility. Due to increasing MnO_2 concentration and temperature, the position of the maximum height of the hump (M''_{max}) shifts towards higher frequency, thus increasing the value of the relaxation frequency

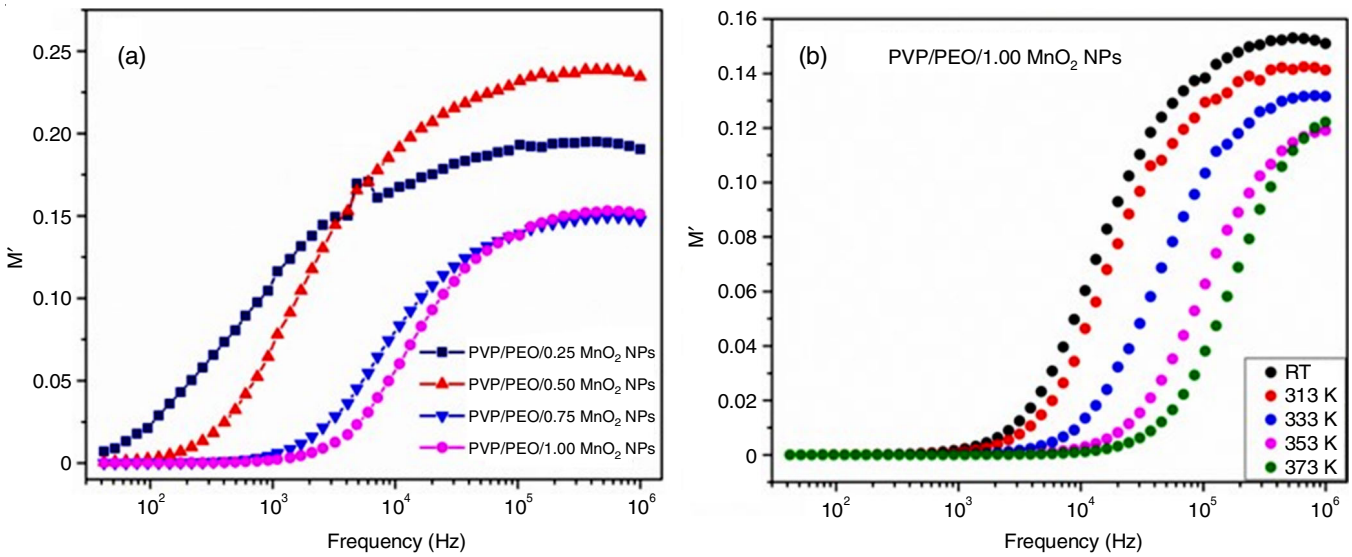

Fig. 6. Real modulus of PEO/PVP/0.25 to 1 wt.% MnO_2 electrode film (a) at 303 K and (b) PEO/PVP/1 wt.% MnO_2 electrode film at various temperature

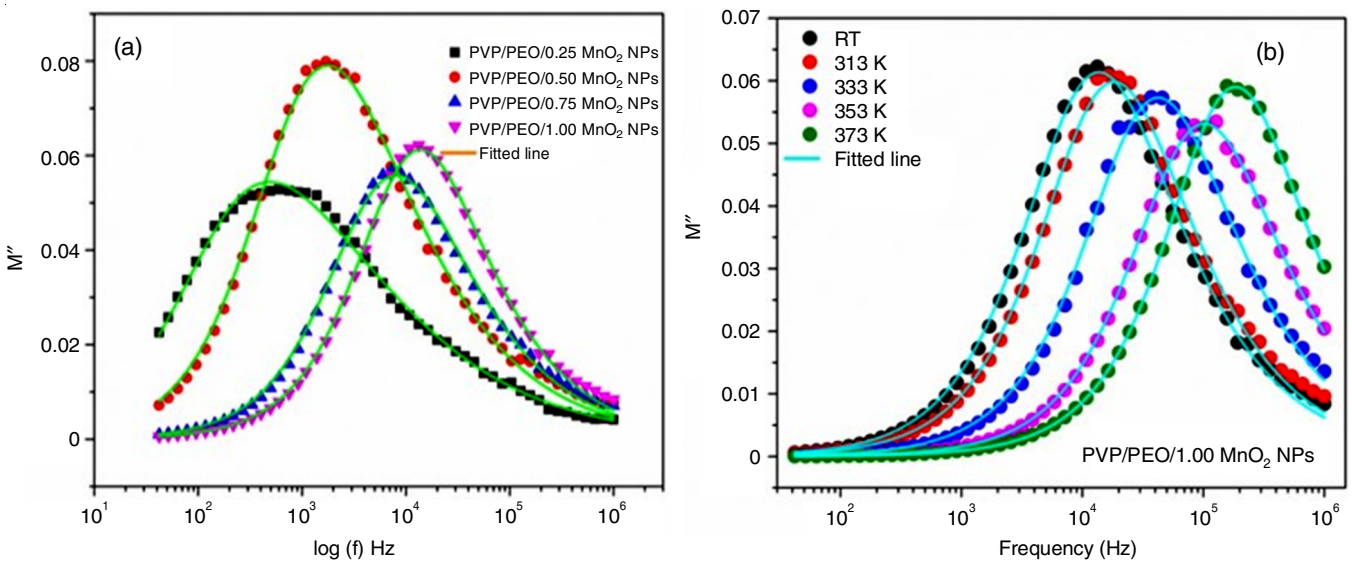

Fig. 7. Imaginary modulus of PEO/PVP/0.25 to 1 wt.% MnO_2 electrode film (a) at 303 K and (b) PEO/PVP/1 wt.% MnO_2 electrode film at various temperature

(f_{max}). Since relaxation frequency and relaxation time (τ) are inversely proportional quantities, τ decreases drastically as the value of f_{max} increases. The asymmetric broadening of M″ plot confirms the non-Debye type relaxation, which was also proved by modified Kohlrausch-Williams-Watts (KWW) function as proposed by Bergman [21]:

$$M'' \frac{M''_{max}}{(1-\beta)+\frac{\beta}{1+\beta}\left[\beta\left(\frac{f_{max}}{f}\right)+\left(\frac{f}{f_{max}}\right)^{\beta}\right]}$$

The value of stretch coefficient (β) is 1 for an ideal Debye type relaxation and $0 < \beta < 1$ for non-Debye type relaxation. The resultant value of β was measured by fitting of KWW function in the M″ data and is listed in Table-2. This result confirms the nature of non-Debye relaxation.

TABLE-2
KWW PARAMETERS FOR VARIOUS (0.25 to 1) wt.% MnO_2 AND 1 wt.% MnO_2 BASED POLYMER ELECTRODE FILM AT ROOM TEMPERATURE AND VARIOUS TEMPERATURE

Resultant values of KWW for 30 wt.% PEO/70 wt.% PVP/X wt.% MnO_2 at 303 K			
X wt.% MnO_2 sample	M''_{max}	f_{max} (Hz)	β
0.25	0.054	489.57	0.486
0.50	0.079	1764.45	0.598
0.75	0.056	8028.62	0.671
1.00	0.061	13819.95	0.729
Resultant values of KWW for 50 wt.% PEO/50 wt.% PVP/1 wt.% MnO_2 sample at different temperature			
Temperature	M''_{max}	f_{max} (Hz)	β
313	0.059	18326.48	0.740
333	0.057	42353.16	0.742
353	0.053	102020.9	0.754
373	0.059	185382.5	0.798

Complex modulus spectra: Semicircle complex modulus spectra is exposed in Fig. 8a-b of PEO/PVP/0.25 to 1 wt.% MnO_2 at room temperature and PEO/PVP/1 wt.% MnO_2 electrode film at different temperature, respectively. The complex modulus spectra is more effective than the complex impedance spectra. Because, modulus formalism can elucidate the relaxation effect of grains by relaxing grain boundaries in nanostructured materials. The presence of one semicircle in the complex modulus spectra indicates that a single relaxation process is possible in the sample. There are numerous explanations for the distribution of relaxation times in solids, including the ellipsoidal form of polar groups, interfacial effects, hopping, occurrence of inhomogeneities. In addition, when temperature rises, the modulus spectra (Fig. 8b) exhibit a shifting towards the origin. It implies that probable change in capacitance values in relation to temperature [22].

Electrochemical studies of fabricated asymmetric supercapacitors: The supercapacitance performances of fabricated (PVP/PEO/X wt.% MnO_2)//activated carbon (AC) asymmetric supercapacitors (ASCs) devices were studied by cycle voltammetry (CV), galvanostatic charge-discharge and electrochemical impedance spectroscopy techniques. Fig. 9a-d shows the CV profiles of ASCs device at various scan rate ranging from 5 to 100 mV s^{-1}. Even at a high scan rate of 100 mV s^{-1}, all CV curves for all ASCs devices were non-rectangle in shape, indicating that all the PNC electrodes have strong capacitive properties. Fig. 9e shows a comparison of CV profiles with a scan rate of 100 mV s^{-1}. The specific capacitance of the ASC device was estimated using the following equation:

$$C_{sp} = \frac{\int IdV}{m \times \Delta V \times \nu}$$

The calculated specific capacitance values of ASC devices are given in Table-3. The C_{sp} value is increased in the order 0.25 wt.% < 0.5 wt.% < 0.75 wt.% < 1 wt.% of MnO_2 nanoparticles in blended PVP/PEO polymer matrix. As the ion diffusion coefficient increases, the ion interaction intensifies on the surfaces of greater wt.% MnO_2 nanoparticles. The intercalation/de-intercalation reaction was more easily observed in the higher

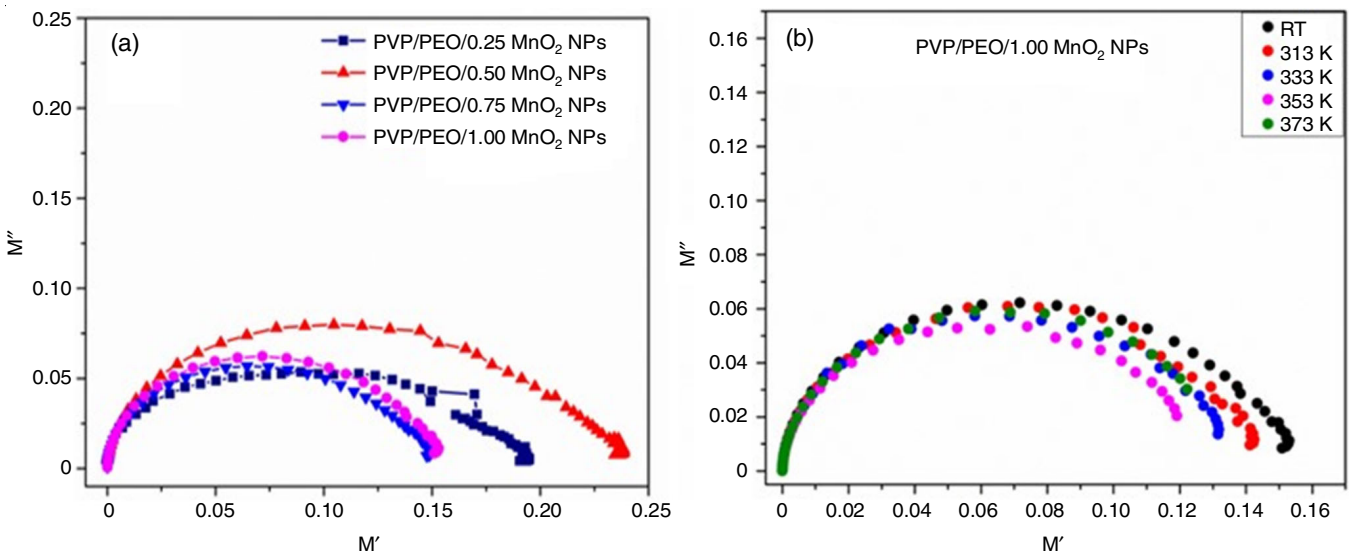

Fig. 8. Complex modulus spectra of PEO/PVP/0.25 to 1 wt.% MnO_2 electrode film (a) at 303 K and (b) PEO/PVP/1 wt.% MnO_2 electrode film at various temperature

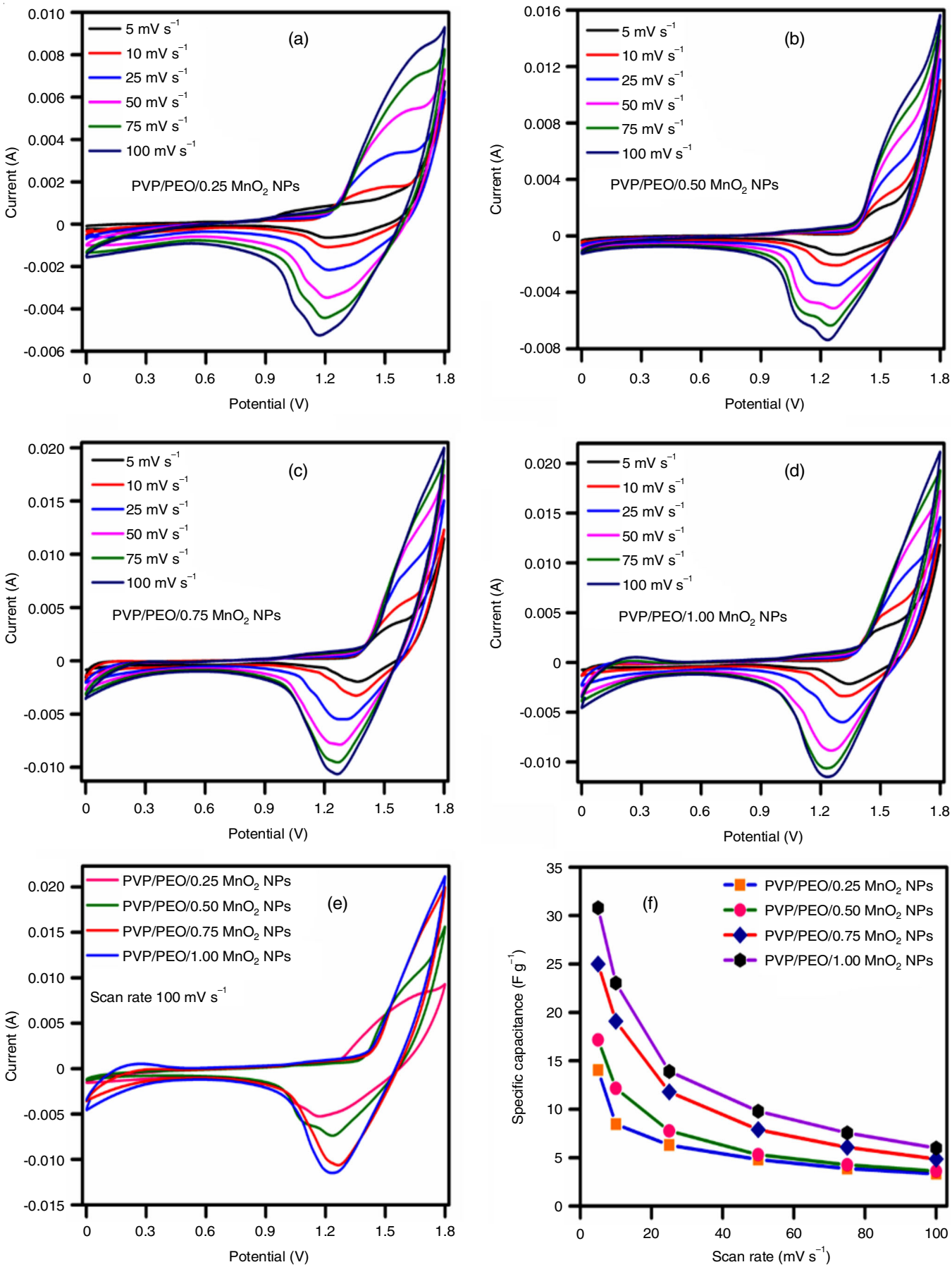

Fig. 9. (a-d) CV profiles of MnO_2 PNC, (e) CV profiles in similar scan rate and (f) Csp of PNC

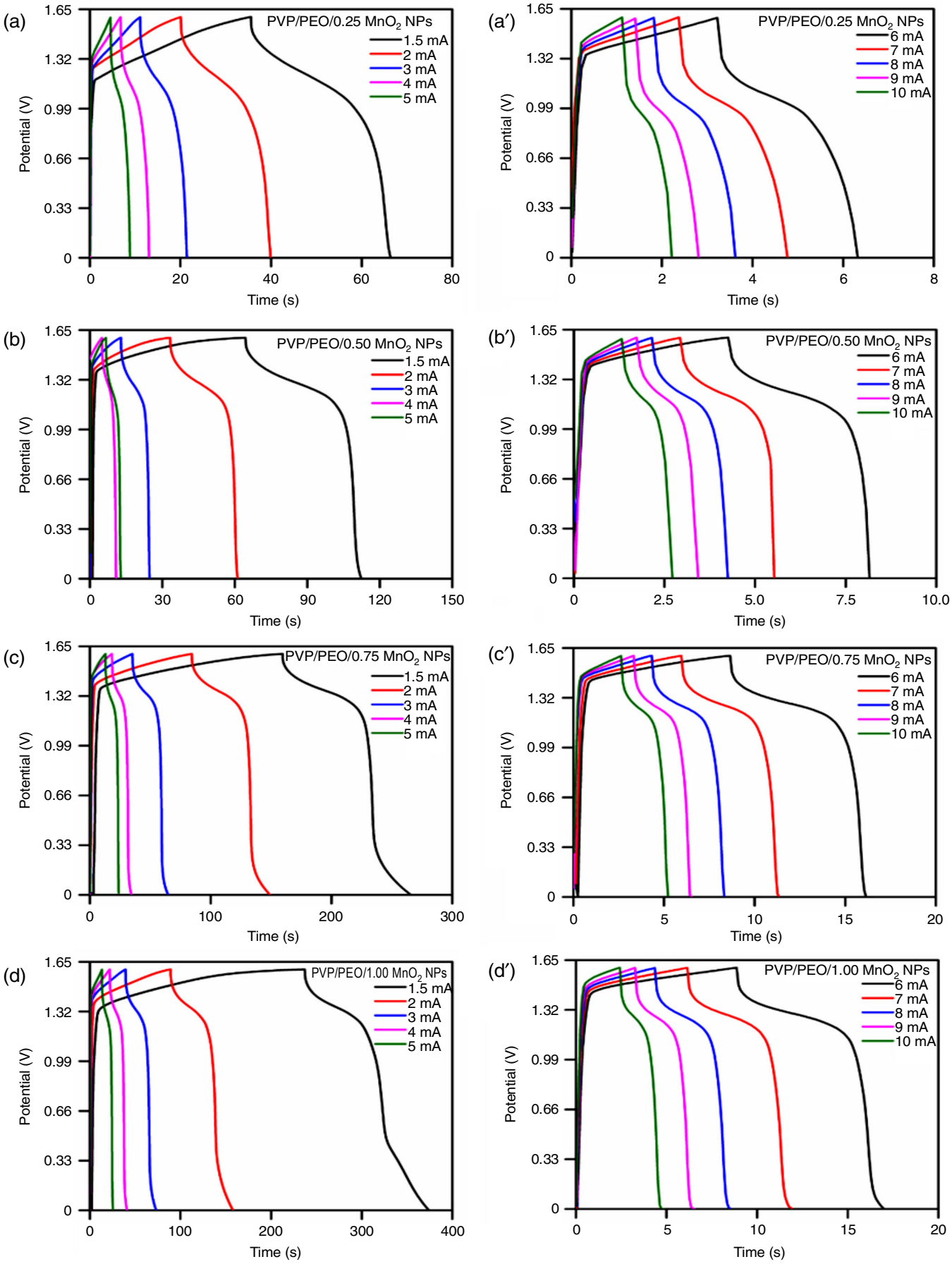

Fig. 10. GCD profiles of ASCs device

TABLE-3
SPECIFIC CAPACITANCE OF ASCs DEVICE AT DIFFERENT SCAN RATE

Scan rate (mV s^{-1})	Specific capacitance (F g^{-1})			
	PVP/PEO/ 0.25 wt.% MnO_2	PVP/PEO/ 0.5 wt.% MnO_2	PVP/PEO/ 0.75 wt.% MnO_2	PVP/PEO/ 1 wt.% MnO_2
5	14.03	17.17	24.99	30.79
10	8..46	12.15	19.09	23.04
25	6.29	7.76	11.79	13.92
50	4.82	5.32	7.89	9.81
75	3.86	4.27	6.08	7.56
100	3.34	3.62	4.85	5.99

wt.% of MnO_2 based polymer nanocomposite electrode [4,8], increasing the pseudocapacitance nature and yielding improved C_{sp} values. Fig. 9f depicts the specific capacitance of an ASC device.

Using chrono-potentiometry, the charge/discharge investigations of the ASCs device in KOH electrolytes were examined at varied current densities of 1.5 to 10 mA, respectively, within a potential range of 0 to 1.6 V. The GCD profiles of the ASCs devices are displayed in Fig. 10. The nonlinear charge distribution is evident, indicating a pseudocapacitive property. Because of the electrode polarization at this high current rate, a potential drop is observed as the electric current reverses from charging to discharging [2]. The GCD profiles of all ASC devices are compared in Fig. 11a and it is evident that the greater the weight percentage of MnO_2 nanoparticles, the longer the discharge time observed in the other weight percentage of nanoparticles. The electrochemical redox reaction at the electrode/electrolyte interface is the cause of the typical pseudocapacitive behaviour of ASCs devices as suggested by the slope fluctuations of the time dependence discharge curve [23]. The electrode demonstrates significant electrochemical reversibility and a rapid I-V response shown by the GCD curves, which have relatively linear and symmetrical shapes and fewer detectable IR dip [24]. Additionally, when current densities rise, the discharge times shorten, suggesting strong rate capacity. Specific capacitance (C_{sp}) and coulomb efficiency (η%), two electrical characteristics, are computed using below equations:

$$C_{sp} = \frac{I \times \Delta t}{m \times \Delta V}$$

$$C_{sp} = \frac{t_d}{t_c} \times 100$$

where m is the mass of active materials; t_c is the charging time; $\Delta t/t_d$ is the discharging time and ΔV is the window potential. Table-4 lists the computed C_{sp} values of ASC device, whereas Fig. 11b displays the specific capacitance of the ASC device at various current densities. Fig. 12a shows the long-term cyclic stability of ASCs device. After 10,000 GCD cycles, the specific capacitance was retained at 89.85% (0.25 wt.% MnO_2), 90.65% (0.5 wt.% MnO_2), 91.56% (0.75 wt.% MnO_2) and 91.89% (1 wt.% MnO_2). The electrode material shrinks and swells during the charge-discharge process, which causes the volume change and mechanical degradation and can be attributed to the poor performance [25-27]. Moreover, the equation was used to determine the ASCs device's coulombic efficiency. Following 10,000 GCD cycles, the computed coulombic efficiency is 99.63%, 99.65%, 99.65% and 99.85% for PVP/PEO/0.25 wt.% MnO_2, PVP/PEO/0.5 wt.% MnO_2, PVP/PEO/0.75 wt.% MnO_2 and PVP/PEO/1 wt.% MnO_2 in that order. The following equations were used to determine the energy and power density of polymer nanocomposite (ASCs device).

$$E = \frac{1/2 \times C_{sp} \times \Delta V^2}{3.6}$$

$$P = \frac{E \times 3600}{\Delta t}$$

where C_{sp} is the specific capacitance (F g^{-1}) of ASCs device; ΔV is the window potential (V); Δt is the discharge duration (s) and E is the energy density (Wh kg^{-1}). Ragone plots of the (PVP/PEO/X wt.% MnO_2)//AC ASCs device are shown in Fig. 12b. The PVP/PEO/1 wt.% MnO_2 polymer nanocomposite, which has a predicted superior energy density of 5.81 Wh kg^{-1} and a power density of 1012.65 W kg^{-1}.

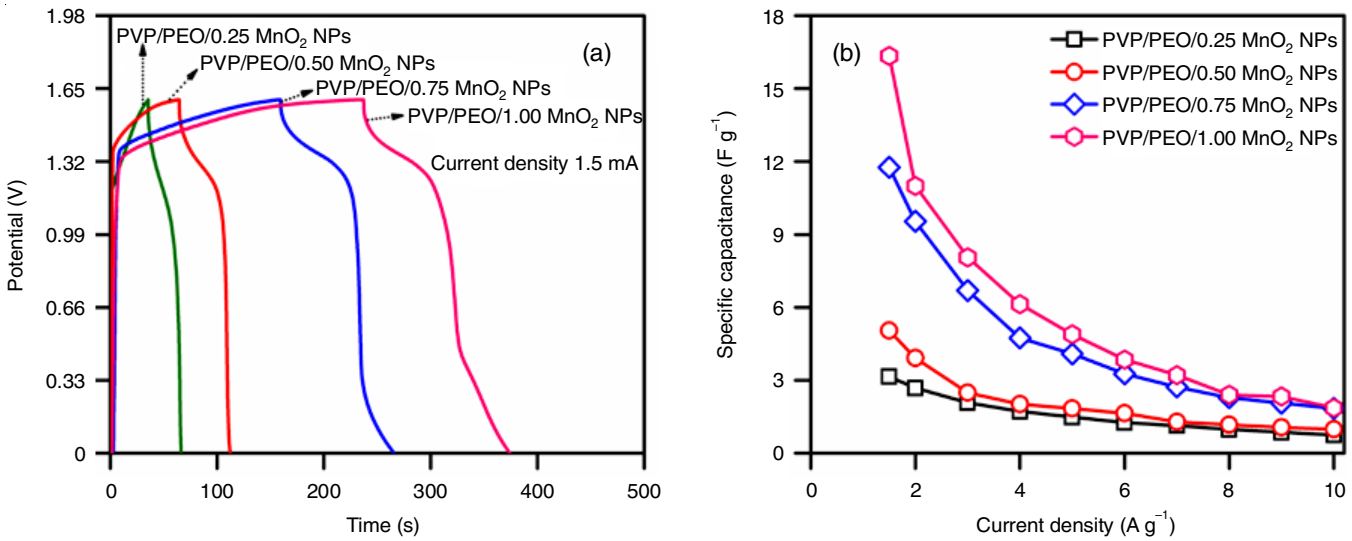

Fig. 11. (a) Comparison of GCD profiles and (b) specific capacitance *vs.* current density

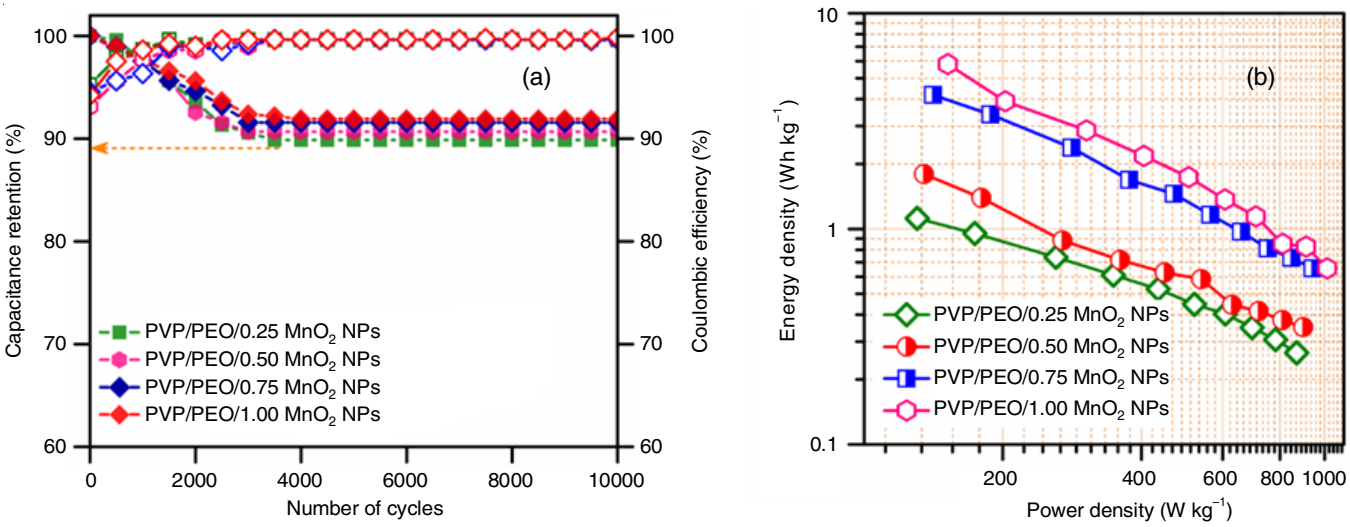

Fig. 12. (a) Capacitance retention with coulombic efficiency and (b) Ragone plot of ASC device

TABLE-4
SPECIFIC CAPACITANCE OF ASCs DEVICE AT DIFFERENT CURRENT DENSITY

Scan rate (mV s^{-1})	Specific capacitance (F g^{-1})			
	PVP/PEO/ 0.25 wt.% MnO_2	PVP/PEO/ 0.5 wt.% MnO_2	PVP/PEO/ 0.75 wt.% MnO_2	PVP/PEO/ 1 wt.% MnO_2
1.5	3.14	5.04	11.76	16.34
2	2.67	3.91	9.53	10.99
3	2.07	2.48	6.69	8..05
4	1.71	2.01	4.74	6.12
5	1.47	1.83	4.08	4.88
6	1.25	1.64	3.26	3.84
7	1.13	1.28	2.72	3.21
8	0.97	1.16	2.28	2.39
9	0.86	1.06	2.06	2.32
10	0.74	0.98	1.84	1.86

The equivalent series resistance (ESR) and frequency response of electrochemical supercapacitors can be effectively evaluated using electrochemical impedance spectroscopy (EIS). Fig. 13 shows the EIS spectra of ASCs devices that were studied in a room temperature KOH electrolyte, spanning a frequency range of 100 kHz to 1 Hz. The semicircle at higher frequency region is ascribed to charge transfer process at electrode/electrolyte interface, whereas the straight line at low-frequency region suggests diffusive of the electrolyte [28]. The inset of Fig. 13 shows the analogous circuit (Z-view fit software) that was used to fit the impedance plot (before and after GCD 10000 cycles). The EIS data was fitted using a series resistance R1, which was calculated from the real axis intercepts at high frequency and is consistent with the resistance of almost all electrolyte solutions. The resistance to electron transport at the interface between the electrolyte and electrode is denoted by R2. Table-5 displays the R_s and R_{ct} values of ASCs devices.

Conclusion

A hybrid nanocomposite PVP/PEO with various weights of MnO_2 was prepared *via* the solution casting method. The structural features and formation of PNCs were confirmed by FTIR and XRD analyses. Increasing the material wt.% of MnO_2 will improve charge carrier availability, hence elevating the conductivity of material. The conductivity of 1 wt.% MnO_2 PNCs increases with increases in temperature due to the thermally activated conduction mechanisms. This is due to the polar nature of the PVP polymer as well as the fact that the hydroxyl group on the chain interacts with water molecules in order to boost the specific capacitance. The charge/discharge process of device in KOH electrolytes was investigated using chronopotentiometry from a 0 to 1.6 V potential window at different current densities of 1 to 10 A g^{-1}. Furthermore, the specific capacitance retained was 89.85%, 90.65%, 91.56% and 91.89% after GCD 10,000 cycles. The fabricated (PVP/PEO/1 wt.% MnO_2)//AC ASCs device has exhibits a superior energy density of 5.81 Wh kg^{-1} and power density of 1012.65 W kg^{-1}.

TABLE-5
R_s AND R_{ct} VALUES OF BEFORE AND AFTER GCD 10000 CYCLES

ASC device	Resistance (Ω)			
	Before GCD		After GCD	
	R_s	R_{ct}	R_s	R_{ct}
PVP/PEO/0.25 wt.% MnO_2	7.36	1.81	7.81	2.26
PVP/PEO/0.25 wt.% MnO_2	4.74	0.85	7.79	1.37
PVP/PEO/0.25 wt.% MnO_2	4.15	0.74	4.21	0.92
PVP/PEO/0.25 wt.% MnO_2	3.44	0.69	4.05	0.76

CONFLICT OF INTEREST

The authors declare that there is no conflict of interests regarding the publication of this article.

REFERENCES

1. C.I. Idumah, *Curr. Res. Green Sustain. Chem.*, **4**, 100173 (2021); https://doi.org/10.1016/j.crgsc.2021.100173
2. A. Murugan, V. Siva, A. Shameem and A.G. Al-Sehemi, *J. Mater. Sci. Mater. Electron.*, **35**, 1041 (2024); https://doi.org/10.1007/s10854-024-12785-0
3. Q. Wang, C. Han, G. Tang, L. Liu, T. Li and Y. Han, *J. Alloys Compd.*, **931**, 167510 (2023); https://doi.org/10.1016/j.jallcom.2022.167510

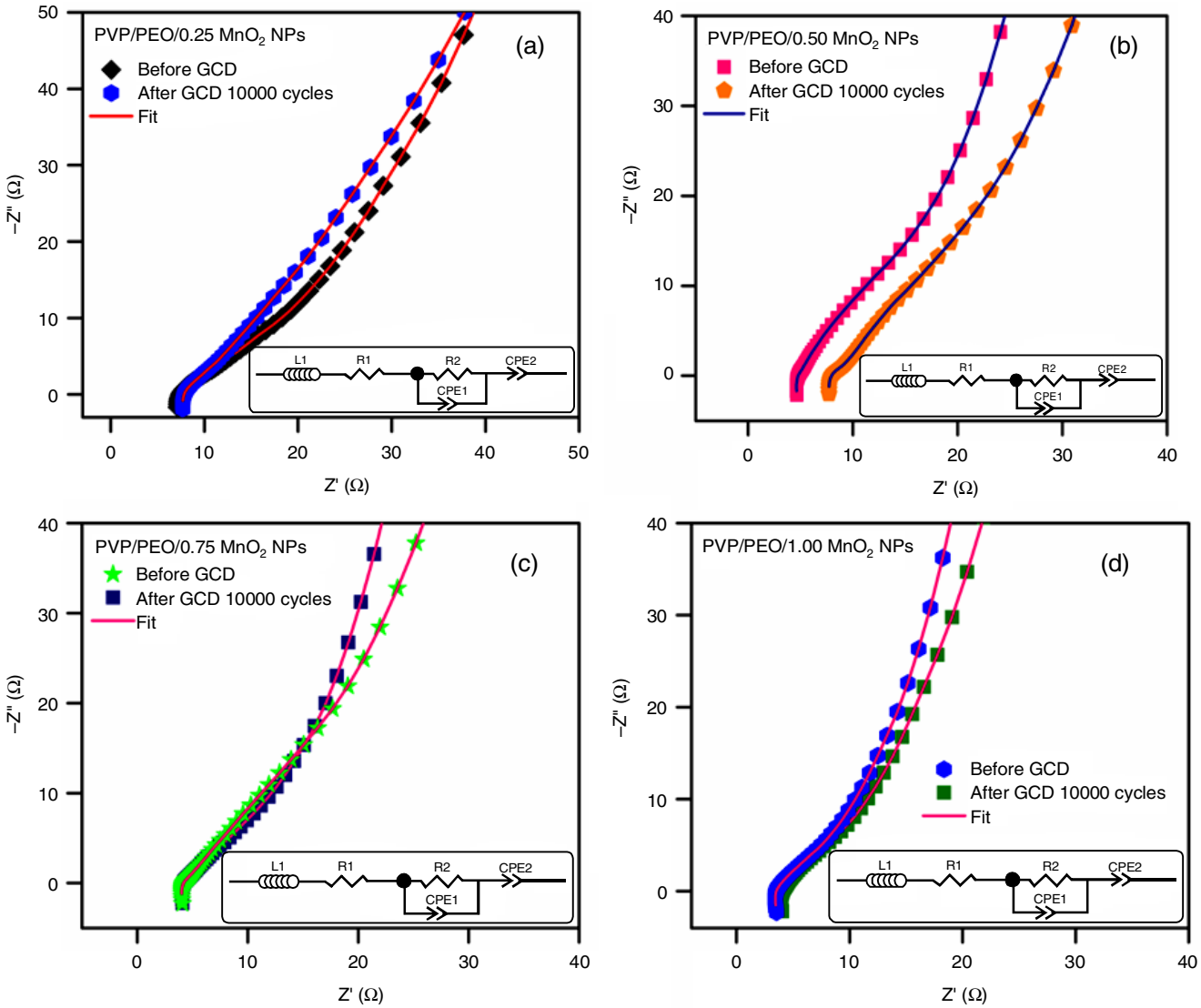

Fig. 13. (a-d) EIS spectra of before and after GCD 10000 cycles and inset shows in an equivalent circuit

4. V. Siva, A. Murugan, A. Shameem, M.A. Jothi and S. Kannan, *Inorg. Chem. Commun.*, **154**, 110986 (2023); https://doi.org/10.1016/j.inoche.2023.110986
5. B. Wang, Q. Liu, D. Sun, M. Liu, Y. Lu, X. Liu, L. Yang, Y. Wang, M. Li and D. Wang, *J. Alloys Compd.*, **982**, 173686 (2024); https://doi.org/10.1016/j.jallcom.2024.173686
6. S.S. Chandraraj and J.R. Xavier, *Surf. Interfaces*, **36**, 102515 (2023); https://doi.org/10.1016/j.surfin.2022.102515
7. G.A. Tafete, M.K. Abera and G. Thothadri, *J. Energy Storage*, **48**, 103938 (2022); https://doi.org/10.1016/j.est.2021.103938
8. W.M.T. Ramya, V. Siva, A. Murugan, A. Shameem, S. Kannan and K. Venkatachalam, *J. Polym. Environ.*, **31**, 1610 (2023); https://doi.org/10.1007/s10924-022-02695-9
9. C. Devi, J. Gellanki, H. Pettersson and S. Kumar, *Sci. Rep.*, **11**, 20180 (2021); https://doi.org/10.1038/s41598-021-99663-5
10. H.M. Alghamdi and A. Rajeh, *Sci. Rep.*, **14**, 18925 (2024); https://doi.org/10.1038/s41598-024-69982-4
11. J. Rodriguez-Romero, I. Ruiz de Larramendi and E. Goikolea, *Batteries*, **8**, 263 (2022); https://doi.org/10.3390/batteries8120263
12. Y. Kumar, S. Chopra, A. Gupta, Y. Kumar, S.J. Uke and S.P. Mardikar, *Mater. Sci. Energy Technol.*, **3**, 566 (2020); https://doi.org/10.1016/j.mset.2020.06.002
13. P.V.M. Dixini, B.B. Carvalho, G.R. Gonçalves, V.C.B. Pegoretti and M.B.J.G. Freitas, *Ionics*, **25**, 4381 (2019); https://doi.org/10.1007/s11581-019-02995-6
14. K.M. Anilkumar, B. Jinisha, M. Manoj and S. Jayalekshmi, *Eur. Polym. J.*, **89**, 249 (2017); https://doi.org/10.1016/j.eurpolymj.2017.02.004
15. A. Bendahhou, K. Chourti, R. El Bouayadi, S. El Barkany and M. Abou-Salama, *RSC Adv.*, **10**, 28007 (2020); https://doi.org/10.1039/D0RA05163B
16. J.T. Heath, J.D. Cohen and W.N. Shafarman, *J. Appl. Phys.*, **95**, 1000 (2004); https://doi.org/10.1063/1.1633982
17. N. Murali, S.J. Margarette, V. Kondala Rao and V. Veeraiah, *J. Sci. Adv. Mater. Devices*, **2**, 233 (2017); https://doi.org/10.1016/j.jsamd.2017.04.004
18. S.O. Tan, O. Çiçek, Ç.G. Türk and S. Altindal, *Eng. Sci. Technol., An Int. J.*, **27**, 101017 (2022); https://doi.org/10.1016/j.jestch.2021.05.021
19. V. Siva, D. Vanitha, A. Murugan, A. Shameem and S.A. Bahadur, *Compos. Commun.*, **23**, 100597 (2021); https://doi.org/10.1016/j.coco.2020.100597
20. S. Kumar, Ravikant, R. Kurchania and A. Kumar, *Ceram. Int.*, **45**, 17137 (2019); https://doi.org/10.1016/j.ceramint.2019.05.267

21. R. Bergman, *J. Appl. Phys.*, **88**, 1356 (2000); https://doi.org/10.1063/1.373824
22. M. Halder and A.K. Meikap, *Rev. Adv. Mater. Sci.*, **59**, 425 (2020); https://doi.org/10.1515/rams-2020-0040
23. S.M. Ingole, S.T. Navale, Y.H. Navale, I.A. Dhole, R.S. Mane, F.J. Stadler and V.B. Patil, *J. Solid State Electrochem.*, **21**, 1817 (2017); https://doi.org/10.1007/s10008-017-3557-8
24. W. Li, H. Xu, M. Cui, J. Zhao, F. Liu and T. Liu, *Ionics*, **25**, 999 (2019); https://doi.org/10.1007/s11581-018-2767-0
25. P. Mishra, S. Sharma and R. Jain, *J. Indian Chem. Soc.*, **94**, 1 (2017).
26. S. Ahmed, A. Ahmed, D.B. Basha, S. Hussain, I. Uddin and M.A. Gondal, *Synth. Met.*, **295**, 117326 (2023); https://doi.org/10.1016/j.synthmet.2023.117326
27. R.S. Kate, S.A. Khalate and R.J. Deokate, *J. Alloys Compd.*, **734**, 89 (2018); https://doi.org/10.1016/j.jallcom.2017.10.262
28. A. Murugan, V. Siva, A. Shameem, S.A. Bahadur, S. Sasikumar and N. Nallamuthu, *J. Energy Storage*, **28**, 101194 (2020); https://doi.org/10.1016/j.est.2020.101194